Three-dimensional diffuse optical tomography in the parallel plane transmission geometry: Evaluation of a hybrid frequency domain/continuous wave clinical system for breast imaging

J. P. Culver[a),b)] R. Choe, M. J. Holboke, L. Zubkov, T. Durduran, and A. Slemp
Department of Physics and Astronomy, University of Pennsylvania, Philadelphia, Pennsylvania 19104-6396

V. Ntziachristos[b)] and B. Chance
Department of Biochemistry and Biophysics, University of Pennsylvania, Philadelphia, Pennsylvania 19104-6396

A. G. Yodh
Department of Physics and Astronomy, University of Pennsylvania, Philadelphia, Pennsylvania 19104-6396

(Received 12 March 2002; accepted for publication 5 November 2002; published 23 January 2003)

Three-dimensional diffuse optical tomography (DOT) of breast requires large data sets for even modest resolution (1 cm). We present a hybrid DOT system that combines a limited number of frequency domain (FD) measurements with a large set of continuous wave (cw) measurements. The FD measurements are used to quantitatively determine tissue averaged absorption and scattering coefficients. The larger cw data sets (10^5 measurements) collected with a lens coupled CCD, permit 3D DOT reconstructions of a 1-liter tissue volume. To address the computational complexity of large data sets and 3D volumes we employ finite difference based reconstructions computed in parallel. Tissue phantom measurements evaluate imaging performance. The tests include the following: point spread function measures of resolution, characterization of the size and contrast of single objects, field of view measurements and spectral characterization of constituent concentrations. We also report *in vivo* measurements. Average tissue optical properties of a healthy breast are used to deduce oxy- and deoxy-hemoglobin concentrations. Differential imaging with a tumor simulating target adhered to the surface of a healthy breast evaluates the influence of physiologic fluctuations on image noise. This tomography system provides robust, quantitative, full 3D image reconstructions with the advantages of high data throughput, single detector–tissue coupling path, and large (1L) imaging domains. In addition, we find that point spread function measurements provide a useful and comprehensive representation of system performance. [DOI: 10.1118/1.1534109]

Key words: optical tomography, NIR spectroscopy, breast imaging, clinical system

I. INTRODUCTION

Diffuse optical tomography (DOT) enables researchers to translate highly scattered, light signals into clinically meaningful information about human tissue.[1–5] The tomographic approaches are new and should offer substantially improved characterization of lesions compared to transillumination approaches of the past.[6–8] Intrinsic contrast derived from oxy- and deoxy-hemoglobin have been used to differentiate tumors from normal tissue based on vascular signatures.[3,9,10] Extrinsic contrast, for example with existing vascular based agents such as indocyanine green, have exhibited significant tumor contrast enhancement.[5,11] Ultimately, perhaps the most promising optical imaging schemes, may involve targeted agents to select cancer tissue based on peptide and molecular level bindings.[12] The exquisite sensitivity of optical spectroscopy to both intrinsic and extrinsic agents make DOT attractive. However, before clinically optimized optical 3D imaging systems can be realized, several challenges remain to be solved.

The main experimental challenges for DOT relate to the speed and size of the collected data set. Coverage and resolution demand large data sets. Patient movement and physiologic fluctuations necessitate fast collection speeds. In fact, full coverage tomography of breast requires large data sets for even modest spatial resolution (e.g., $\approx$1 cm). Consider a DOT system that aims to provide 0.2–1.0 cm resolution in deep breast tissue (i.e., depths of 1 to 4 cm) with 1 liter volume coverage. Even if we naively assume that a measurement number equal to the number of voxels is sufficient, we require from 10^3 (1 cm resolution) to 10^5 (0.2 cm resolution) measurements. Furthermore there is often an advantage to oversampling for signal averaging considerations, or for handling surface features that have sub-millimeter structure and are near the regions of high measurement sensitivity.[13] Most clinical prototypes used for *in vivo* measurements have had much smaller data sets, in the range of 10^1 to 10^3 optode pairings,[3,5] though recently a few systems with larger data sets have been reported.[2] In this paper we present the results of a comprehensive investigation on the design, optimization and imaging performance of a hybrid DOT system that combines a limited number of frequency domain measurements

(720) with a significantly larger set of CW measurements (10^5). Before discussing the design in detail we briefly review our design rationale.

Every diffuse optical tomography system must make compromises about data type and number, measurement geometry, optode placement, and reconstruction method. Generally for absorption and scattering images there are three possible measurement approaches; time domain (pulsed input light with pulse duration $\tau_p \approx 100$ ps), frequency domain (modulated input light with frequency $\omega \approx 10^6 - 10^9$ Hz), and continuous-wave ($\omega \approx DC - 100$ kHz). The time domain approach yields the most information per optode pair when the signal-to-noise ratio is sufficiently large, but it is usually the most expensive technique per optode pair. Continuous-wave (cw) measurements on the other hand are the least expensive and yield the least information per optode pair. Within the diffusion approximation the tissue is described by space- and time-dependent absorption and scattering coefficients and index of refraction.[14] To extract and separate variables at a single light wavelength a system needs at least three independent measures[15] (for example, multiple frequency domain or a time domain measurements). On a per-optode basis the frequency–domain and time-resolved measurements would seem to have an advantage over the cw approach. However, in practice it is possible to reduce the number of time-independent measurements needed by making assumptions about the medium such as its absorption and scattering properties. Imaging of differential changes can also dramatically improve the robustness of reconstruction.[16]

The most popular geometry for breast imaging has been the 2D circular array of sources and detectors.[17–21] This geometry is appealing, in part because of its similarity to the geometries used for computer aided tomography. It benefits from a full 2D measurement view over the entire circumference of the tissue volume. Full exploitation of this geometry requires large dynamic range and large channel separation so that the high light intensities at the close distances do not contaminate the low light levels (10^{-6} lower) at the long source detector separations. Another attractive geometry, which builds on experience with conventional mammography is the planar geometry which has been employed in both parallel scanning modes[9,22] and limited view DOT arrangements.[5,23] The disadvantage of this geometry is that the view is limited. It does not fully surround the surface of the tissue volume. An advantage is that the tissue is compressed providing increased light transmission and increased resolution, since resolution performance falls off with distance from the measurement surface.[13,23–25] In addition, in the parallel plate transmission mode the dynamic range requirements of the detection system are reduced, and the mechanics of adapting to different breast size is reduced to a simple planar translation analogous to traditional x-ray mammography.

With these considerations in mind, we have pursued a hybrid frequency domain/continuous wave approach with massively parallel detection via a lens coupled CCD camera. The frequency domain (FD) measurements enable us to quantitatively determine the tissue averaged absorption and scattering coefficients and thus to impose constraints on the analysis of the cw data. The larger cw data sets (10^5 measurements) collected with a CCD permit 3D DOT reconstruction of a 1-liter tissue volume. Using a plane parallel transmission geometry the breast surface is imaged via a lens coupled CCD. This scheme reduces the complexity of the light channeling system to a single lens, instead of an array of fibers. For extrinsic contrast agents this is a natural imaging approach that has not been pursued to the clinical prototype by others.

Some form of optical tomography or image reconstruction must play a central role in any system which aims to use diffuse light to improve breast tumor diagnosis. Indeed the weakness in early (and current) clinical work is at least partially attributable to deficiencies in the image reconstruction approach. Various reconstruction approaches exist for DOT, (for a review see Arridge[26]). In this work we employ a finite difference forward solver and use the explicit adjoint formulation for the inverse problem as described below. Most DOT approaches have been implemented in two dimensions. In the best 2D cases, researchers have employed a cylindrical geometry to reduce the dimensionality of the problem.[17–21,27] Recently there have been direct comparisons between full 3D and 2D reconstructions using simulated data;[17,19,28] not surprisingly the 3D reconstructions were superior. The main barrier for full 3D reconstruction is the significant memory and processing time it requires. For example, with 0.125 mL voxels, 1 L imaging domain, 10,000 measurements and a single 500 MHz, Pentium III processor our reconstructions take 24 h. These numbers can vary by up to an order of magnitude depending on details of the algorithm. There are two steps of the algorithms that are costly: (1) solving the forward problem for each source position, detector position and/or frequency, (2) solving the inverse problem. We have chosen to solve these large-scale computational problems using parallel computing[10] which reduces our reconstruction time from 24 h to 2 h.

The paper proceeds as follows. In the methods section we describe the experimental setup, the image reconstruction procedure, data analysis methods, tissue phantom experiments and *in vivo* measurement procedures. In the results and discussion section we evaluate and develop the relation between image noise and resolution for the system. We then proceed to evaluate object characterization, multiple object tomography, field of view and spectral decomposition of multiple absorption images into constituent properties. One of the significant challenges to imaging tumors is the heterogeneous nature of healthy breast tissue. Shah *et al.*[29] have reported spatial variations in μ_s' over tumor and healthy breast tissue. Quaresima *et al.*[30] reported spatial variations in μ_a. To assess the effects off heterogeneous optical properties on imaging focal objects we performed phantom studies with healthy subjects. *In vivo* results are discussed including measures of tissue averaged optical properties and differential imaging with a tumor simulating target in the presence of tissue spatial heterogeneity and temporal fluctuations.

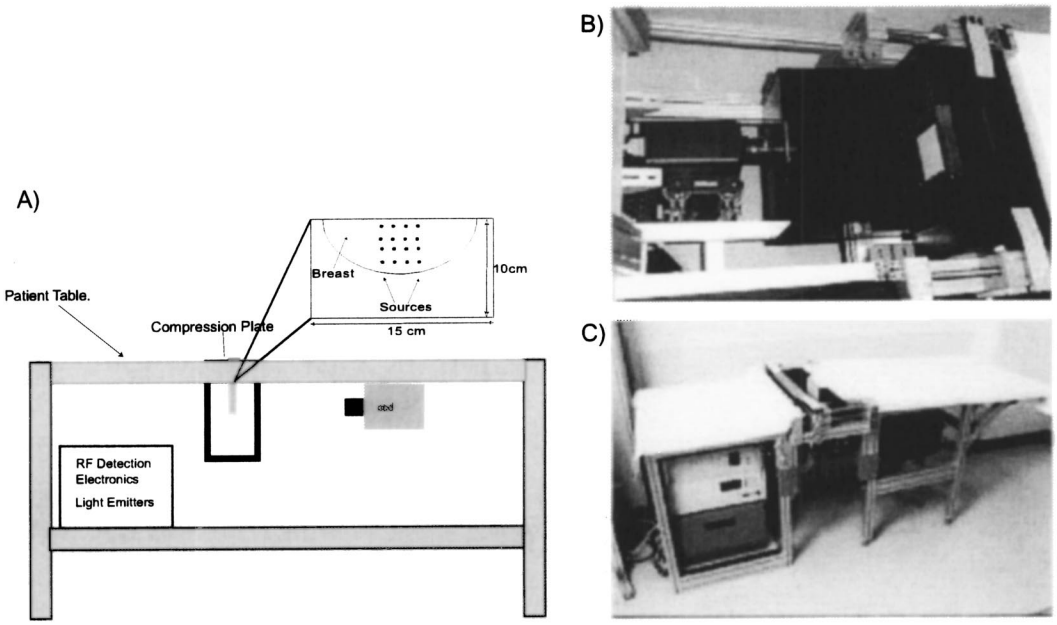

FIG. 1. (a) Schematic of a clinical DOT table. (b), (c) Pictures of the instrument. The subject lies on the table with both breasts suspended in the Intralipid tank and positions one breast central to the measurement area. The breast is held in soft compression between a movable compression plate and viewing window. Laser light sources are optically switched between 45 fibers arranged on in a 9×5 square lattice within the compression plate. The modular viewing window can be fitted with either diffuse or anti-reflective coated transparent windows. The transmitted light is detected by a TE cooled, 2.6 cm×2.68 cm, lens coupled CCD. Simultaneous frequency domain measurements are made with an array of 9 detectors fibers interlaced among the source fibers in the compression plate.

II. METHODS

A. Experimental

1. CCD transmission data

In Fig. 1 we illustrate our clinical diffuse optical tomography table. For human measurements the subject lies on the table with both breasts suspended in a tank filled with the Intralipid. One breast is positioned central to the measurement area and held in soft compression between a movable compression plate and the viewing window. Four lasers operating at 690 nm, 750 nm, 786 nm, and 830 nm, respectively, are optically switched (Dicon Fiber Optics, GP700) between 45 fibers arranged on in a 9×5 square lattice within the compression plate. The switching times are <100 ms between colors, and <500 ms between source positions. The laser powers are balanced so typically 600±200 μW is delivered to the fiber tips for each of the four colors.

The viewing window is modular and permits use of diffuse or anti-reflective coated transparent windows. A 50 mm F#=1.4 lens (Nikkor AF 50 mm F/1.4D) is used to image the detection plane onto the CCD chip with a magnification of 0.2. The light is detected by a thermoelectrically cooled (−40 °C) 1300×1340 CCD pixel array with area 2.6 cm ×2.68 cm (Roper Scientific, NTE1340). The CCD array is read with 16 bit A/D conversion. With a 800×1120 pixel ROI and 2×2 on chip binning the readout time is 300 ms. With a 1 second exposure time the dark count was ~115±11 counts per 2×2 pixel bin. A dark count image was taken and subtracted from each measurement image. Background room light was reduced to levels below the standard deviation in the dark image (~11 counts) using a long pass color glass filter (670 nm, CVI Laser Inc.) placed in front of the CCD lens, and a light shielding box surrounding the camera. Frequency domain measurements are made with an array of 9 detectors fibers interlaced among the source fibers in the compression plate. The same lasers are used for both the frequency domain and the CCD measurements and they are detected simultaneously. The total scan time for all 45 sources is 3 minutes for one color and 12 minutes for 4 colors.

The signal-to-noise ratio (SNR) of the CCD light intensity measurements was evaluated using Intralipid tissue phantoms with a range of different source detector plane distances (ΔY_{sd}). CCD measurements were binned into 24×24 square units to given an equivalent pixel size of 0.35 cm×0.35 cm on the breast surface. A series of 100 measurements with 1 second exposure times were made on tissue phantoms with ($\mu_a = 0.05$ cm^{-1} and $\mu_s' = 10$ cm^{-1}). The noise across the image plane was defined as the standard deviation for each binned pixel. For the source–detector plate separations of $\Delta Y_{sd} = 5$ to 7 cm, the SNR was greater than 10^3 for the peak signal pixel (i.e., the pixel with the shortest source–detector separation). For lower light level pixels with light intensity 1% the peak intensity, (corresponding to a 6 cm displacement on the detection plane from the peak signal pixel), the SNR was 10^3 for $\Delta Y_{sd} = 6$ cm and 10^2 for $\Delta Y_{sd} = 7$ cm. When the optical switch is switched between each frame the maximum SNR decreases to 2×10^2. In our *in vivo* measurements of breast optical properties using a similar geometry most breast compressions were 6±1 cm.[31] Diffuse stray light contamination was present at a level of $\approx 10^{-4} * I_{peak}$. To avoid complications due to this light, data was cropped at I/I_{peak}

<0.03, keeping the stray light contribution $\leqslant 1\%$. For typical optical properties and source detector plate separations this intensity threshold cropped the data at a radius of 6 cm from the peak value. For the reconstructions the detector grid was defined as a 21×13 grid of measurements spaced 0.464 cm in both x and z directions spanning the region from $\mathbf{r}_i = \{-4.64 \text{ cm}, y_d, -2.32 \text{ cm}\}$ to $\mathbf{r}_2 = \{4.64 \text{ cm}, y_d, 2.32 \text{ cm}\}$.

2. Frequency domain

The light sources consist of the laser diodes described in the previous section (which are modulated at 70 MHz). Light from the breast surface is channeled through 3 mm fiber bundles and measured by APD's (Hamamatsu C5331-04). The amplitude and phase of the detected diffuse photon density waves are obtained by demodulating the output of the APD using a homodyne technique.[32] In our system the electrical signal from the APD passes through an amplifier (ZFL-500LN Mini-Circuits, gain=24 dB), a band pass filter (BLP-70 Mini-Circuits), a computer controlled digital attenuator [ZFAT -51020 Mini-Circuits (0-36 dB] and another amplifier (ZFL 500HLN, gain=19 dB). An IQ demodulator (ZFMIQ-70D, 70 MHz, Mini-Circuits) followed by a low pass filter (SLP-1.9, Mini-Circuits) extracts phase and amplitude relative to the RF reference signal that drives the lasers. To minimize the cross-talk between various components, all of the elements are placed in NIM boxes. The system is characterized by a noise equivalent power of 3 pW/$\sqrt{(\text{Hz})}$, a linearity in amplitude of 1%, and phase drift of 0.25 degrees over 80 dB.

B. Theory

In this section we describe our forward model for light transport in tissue and our inverse solution scheme.

1. Forward model

We model light propagation through tissue and tissue phantoms with the diffusion approximation,

$$\nabla\cdot(D(\mathbf{r})\nabla\boldsymbol{\phi}(\mathbf{r}))-\left(\mu_a(\mathbf{r})-\frac{\mathbf{i}\omega}{\nu}\right)\phi(\mathbf{r})=-\mathbf{S}(\mathbf{r}). \tag{1}$$

Here $D(\mathbf{r})=1/3(\mu_s'(\mathbf{r}))$ is the diffusion coefficient, $\mu_s'(\mathbf{r})$ is the scattering coefficient. $\phi(\mathbf{r})$ is the photon fluence rate, $\mu_a(\mathbf{r})$ is the absorption coefficient, ν is the speed of light in the media and ω is the source light modulation frequency. The source is characterized by an amplitude and phase [i.e., $S(r)=S_0e^{i\phi_0}\delta(r-r_s)$]. Partial current boundary conditions are used on all surfaces:

$$\frac{\delta\phi(\mathbf{r})}{\delta n}=-\alpha\phi(\mathbf{r}), \tag{2}$$

where $\alpha=(1-R_{\text{eff}})/(1+R_{\text{eff}})\ (3\mu_s'/2)$, where $R_{\text{eff}}\approx -1.440n^{-2}+0.170n^{-1}+0.668+0.063n$ and $n=n_{\text{in}}/n_{\text{out}}$.

The heterogeneous diffusion equation is solved using a finite difference algorithm throughout a rectangular domain.[10] The rectangular volume is defined by $\mathbf{r}_{\text{FV1}}=\{-8,0,-8\}$ and $\mathbf{r}_{\text{FV2}}=\{8,6,8\}$ with elements $\{Nx,Ny,Nz\}=\{65,25,65\}$ of size $\{\Delta x,\Delta y,\Delta z\}=\{0.25,0.25,0.25\}$ cm for a total of 105,625 grid points.

2. Image reconstructions

We describe our reconstruction scheme for absorbing heterogeneities only. Our approach is based on the diffusion equation [Eq. (1)] and involves minimizing a Rytov type least squared error between calculated and measured photon densities for each source detector pair.[33–35] Optode pair measurements (indexed by i) are indicated by the source and detector positions $(\mathbf{r}_{di},\mathbf{r}_{si})$. The error function minimized is (see Engl *et al.*[36])

$$\min\left\{\left\|\left\{\ln\left(\frac{\phi_m}{\phi_{mR}}\right)\right\}-\left\{\ln\left(\frac{\phi_c}{\phi_{cR}}\right)\right\}\right\|_2^2+\text{Regularization}\right\}. \tag{3}$$

The measured photon fluence rates for a reference medium and the medium of interest are $\phi_{mR}(\mathbf{r}_{di},\mathbf{r}_{si})$ and $\phi_m(\mathbf{r}_{di},\mathbf{r}_{si})$, respectively. Similarly $\phi_{cR}(\mathbf{r}_{di},\mathbf{r}_{si})$ and $\phi_c(\mathbf{r}_{di},\mathbf{r}_{si})$ are the respective ''reference'' and ''of interest'' calculated fields. The regularization term is discussed below. $\phi_{cR}(\mathbf{r}_{di},\mathbf{r}_{si})$ is calculated using *a priori* information, (usually the Intralipid mixture optical properties and tank geometry). $\phi_c(\mathbf{r}_{di},\mathbf{r}_{si})$ however is computed based on the unknown properties that we wish to determine; its calculation requires inversion techniques.

To determine $\phi_c(\mathbf{r}_{di},\mathbf{r}_{si})$ we used an iterative model, with linear Rytov update steps. We defined $\phi_c^{k+1}(\mathbf{r}_{di},\mathbf{r}_{si})=\phi_c^k(\mathbf{r}_{di},\mathbf{r}_{si})\exp(\phi_{\text{scat}}^{k+1}(\mathbf{r}_{di},\mathbf{r}_{si}))$, where k is the iteration index and $\phi_c^0(\mathbf{r}_{di},\mathbf{r}_{si})$ is calculated using an initial guess of the optical properties. The Rytov scattered wave for a particular source detector pair, $\phi_{\text{scat}}^{k+1}(\mathbf{r}_{si},\mathbf{r}_{di})$ is thus

$$-\ln\left(\frac{\phi_c^{k+1}(\mathbf{r}_{di},\mathbf{r}_{si})}{\phi_c^k(\mathbf{r}_{di},\mathbf{r}_{si})}\right)=\frac{\nu}{D}\frac{\int G_c^k(\mathbf{r}_{di},\mathbf{r})G_c^k(\mathbf{r},\mathbf{r}_{si})\Delta\mu_a^{k+1}(\mathbf{r})d^3r}{G_c^k(\mathbf{r}_{di},\mathbf{r}_{si})}. \tag{4}$$

Here $\phi_c^k(\mathbf{r},\mathbf{r}_{si})$ is the solution to the diffusion equation for a light source at position $\mathbf{r}_{si}$ and a specified distribution of absorption $\mu_a^k(\mathbf{r})$ and scattering $\mu_s'(\mathbf{r})$. The Green's function $G_c^k(\mathbf{r}_{di},\mathbf{r})$ is the solution to the diffusion equation for a delta function source at the location of the ith detector, $(S=\delta(\mathbf{r}_{di}-\mathbf{r}))$, and the same distributions of absorption, $\mu_a^k(\mathbf{r})$, and scattering, $\mu_s'(\mathbf{r})$. The differential absorption $(\Delta\mu_a^{k+1}(\mathbf{r}))$ is the unknown vector we seek.

Equation (4) can be transformed into the following matrix equation:

$$-\left\{\ln\left(\frac{\phi_c^{k+1}}{\phi_c^k}\right)\right\}=[\mathbf{J^k}]\{\boldsymbol{\Delta}\mu_a^{\mathbf{k+1}}\}^{\mathbf{T}}. \tag{5}$$

The Jacobian $([\mathbf{J^k}]=[\delta\{\ln(\phi_c^{\mathbf{k}})\}/\delta\mu_a])$ is explicitly generated using an adjoint method:

$$\left(\frac{\delta\{\ln(\phi_c^k)\}}{\delta\mu_a}\right)_{ij}=\frac{\nu}{D}\frac{G_c^k(\mathbf{r}_{di},\mathbf{r}_j)G_c^k(\mathbf{r}_j,\mathbf{r}_{si})}{G_c^k(\mathbf{r}_{di},\mathbf{r}_{si})}, \tag{6}$$

where $\mathbf{r}_j$ is the voxel position.

We follow a Morse–Penrose pseudoinverse approach in which a square matrix is created by multiplying both sides of the forward problem by the transpose of the Jacobian. The inversion is stabilized using a spatially variant Tikhonov regularization scheme. With substitution of ϕ_c^{k+1} for ϕ_c the objective function [Eq. (3)] used for each iteration inverse step becomes

$$\min\left\{\left\|\left\{\ln\left(\frac{\phi_m}{\phi_{mR}}\right)\right\}-\left\{\ln\left(\frac{\phi_c^k}{\phi_{cR}}\right)\right\}+[\mathbf{J^k}]\{\mathbf{\Delta}\mu_\mathbf{a}^{\mathbf{k+1}}\}^\mathbf{T}\right\|_2^2+\lambda(\mathbf{r})\|\{\mathbf{\Delta}\mu_\mathbf{a}^{\mathbf{k+1}}\}\|_2^2\right. \tag{7}$$

This can be arranged in a more compact form:

$$\min\left\{\left\|[\mathbf{J^k}]\{\mathbf{\Delta}\mu_\mathbf{a}^{\mathbf{k+1}}\}^\mathbf{T}+\left\{\ln\left(\frac{\phi_\mathbf{m}}{\phi_\mathbf{mR}}\frac{\phi_\mathbf{cR}}{\phi_\mathbf{c}^\mathbf{k}}\right)\right\}\right\|_2^2+\lambda(\mathbf{r})\|\{\mathbf{\Delta}\mu_\mathbf{a}^{\mathbf{k+1}}\}\|_2^2\right\}. \tag{8}$$

The related matrix equation to be inverted for each iteration step is

$$([\mathbf{J^k}]^\mathbf{T}[\mathbf{J^k}]+\lambda(\mathbf{r})[\mathbf{I}])\{\mathbf{\Delta}\mu_\mathbf{a}^{\mathbf{k+1}}\}^\mathbf{T}=-[\mathbf{J^k}]^\mathbf{T}\left\{\ln\left(\frac{\phi_\mathbf{m}}{\phi_\mathbf{mR}}\frac{\phi_\mathbf{cR}}{\phi_\mathbf{c}^\mathbf{k}}\right)\right\}. \tag{9}$$

This matrix equation is solved using a conjugate gradient method. The result of one inverse solve is an updated set of optical properties. The optical property map from the preceding iteration is used as the basis for a finite difference forward solve and construction of the Jacobian for each iteration. The regularization constants defined below were held constant at each step. Convergence was found to be consistently obtained after fifteen iterations.

Following Pogue *et al.*[37] we use spatially variant regularization. We implement the method in the plane parallel geometry using a spatially variant regularization parameter controlled by center (l_c) and edge (l_e) parameters according to the following formula:

$$\lambda(\mathbf{r})=l_c+l_e*(e^{-\rho_x/R_x}+e^{-\rho_y/R_y}+e^{-\rho_z/R_z}-3). \tag{10}$$

Here, $\rho_x=\|r_x\|$, $\rho_y=\|r_y-3\|$, $\rho_z=\|r_z\|$, and $R_x=16$, $R_y=6$, $R_z=16$. A ratio of $l_e/l_c=10$ was empirically determined to produce even image noise as a function of depth from the source and detector planes. Finally, the inversion volume was performed over a mesh volume defined by $\mathbf{r}_{\mathrm{IV1}}=\{-6,0,-6\}$ and $\mathbf{r}_{\mathrm{IV2}}=\{6,\delta Y_{\mathrm{sd}},6\}$ with elements $\{nx,ny,nz\}=\{24,12,24\}$ of size $\{\delta_x,\delta_y,\delta_z\}=\{0.5,0.5,0.5\}$ cm.

C. Phantom measurements

Tissue phantom imaging experiments were used to evaluate the imaging performance of our machine. All phantom tests were performed using a background Intralipid/ink tissue phantom with a $\mu_a(\lambda(786\text{ nm}))=0.05\text{ cm}^{-1}$ and $\mu_s'(\lambda(786\text{ nm}))=8\text{ cm}^{-1}$. Silicon rubber tissue phantoms were used to create solid shapes for two purposes. To avoid problems related to the phenomena of a tissue air interface near our imaging domain, we extended the diffuse media vertically by placing a solid tissue phantom above the compression plate area. When a subject is in the machine, the chest wall plays a similar role. The tissue phantom top used in these measurements had $\mu_a(\lambda(786\text{ nm}))=0.067\text{ cm}^{-1}$ and $\mu_s'(\lambda(786\text{ nm}))=13\text{ cm}^{-1}$. The solid tissue phantoms were also used as imaging targets. The targets were cut from 500 ml homogeneous solid blocks with prescribed optical properties and suspended in Intralipid with thin white thread at prescribed positions.

A final group of indocyanine green (ICG) phantom measurements employed a pair of flow cells. They were cylinders with inside diameter 1.6 cm, inside length 1.6 cm, and wall thickness of 0.05 cm. In general the objects were placed in pairs as depicted in Fig. 2, with positions $\mathbf{r}_{\mathrm{obj1}}=\{-2.5,3,0\}$ and $\mathbf{r}_{\mathrm{obj2}}=\{2.5,3,0\}$.

D. *In vivo* measurements

In vivo measurements evaluated a system performance for obtaining background optical properties of breast tissue, differential imaging in the presence of physiologic fluctuations. All measurements with humans were performed in accordance with University of Pennsylvania IRB protocol, #700394. The tissue averaged optical properties of breast were obtained using frequency domain measurements that predominantly sampled the breast tissue. One healthy subject age 25 was measured. The compressed breast shape was a half ellipsoid measuring 13 cm at the top of the compression plate and extending 10 cm below the top source. A subset of central sources near the four detectors that were more than 2 cm away from the breast/Intralipid boundary were used. The data was analyzed by approximating the breast geometry as a homogeneous slab. We fit the phase and amplitude of the diffuse photon density waves as a function of the source–detector distance (ρ) using an extrapolated zero boundary, semi-infinite media solution.[38,39] The measurement was repeated 10 times.

To evaluate the influence of physiologic fluctuations on image noise, we made differential measurements with and without an ink/silicone target (diameter=1 cm, $\mu_a=0.2\text{ cm}^{-1}$) taped externally to the side of the breast. Background measurements were taken after removing the target. The scattered wave was constructed using $\phi_m=\phi_{\text{target-on}}$ and $\phi_{m0}=\phi_{\text{target-off}}$. The measured breast tissue averaged optical properties were assumed for the entire volume. Although this assumption generates a model mismatch in the Intralipid volume, such assumptions have been shown to be useful simplifications in differential imaging applications.[2,16]

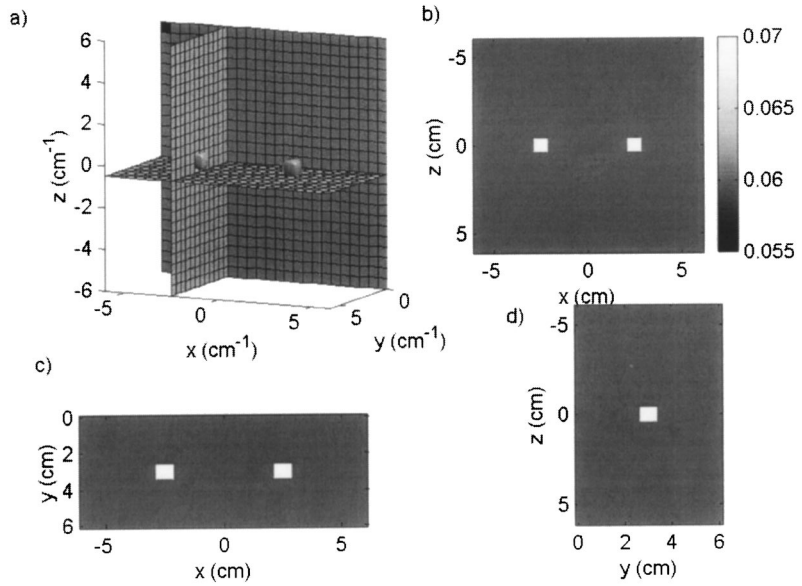

FIG. 2. The schematic of reconstruction volume. Sources are located in the $y=0$ plane the detectors are located on the $y=6$ cm plane. The position of two typical target phantoms is indicated. (a) An isosurface rendering combined with slices through three orthogonal planes. The slices are individually rendered in the following three figures: (b) *xz*-plane slice at $y=2.75$ cm; (c) *xy*-plane slice at $z=0.25$ cm; (d) *yz*-plane slice at $x=-2.5$ cm. Gray scale (units cm^{-1}) for all figures is shown in (b).

III. RESULTS

A. Point spread functions

We evaluated the resolution performance of our system using point spread function (PSF) measurements. In these tests we measured the reconstruction size (FWHM) of point-like objects. For any measurement, the extent of the PSF can be reduced. The cost of better resolution however is increased image noise. Our experiments thus also evaluate the resolution-vs-image noise relation. We used small strongly absorbing point-like objects, specifically 0.4 cm diameter spheres with $\mu_a=2.0$ cm^{-1} and $\mu_s'=8$ cm^{-1}. These objects have a linear signal strength ($\delta\mu_a * volume=0.07$ cm^2) which is similar to the linear signal strength of an object with 1 cm^3 volume and a $\delta\mu_a=0.07$ cm^{-1}. Two such objects were arranged at $\mathbf{r}_1=\{-2.5,3,0\}$, and $\mathbf{r}_2=\{2.3,3,0\}$.

Reconstructions were performed for a range of regularization constants, $l_c=\{1000,100,10,1,0.1,0.01,0.001\}$. Figure 3 depicts a reconstruction with $l_c=0.1$. Plots of object cross-sections and a histogram of the image intensity values for a range of regularization constants (Fig. 4) illustrate the effects of regularization. The cross-sections are evaluated at the FWHM. The dispersion of the image intensities indicate image noise. Generally the histogram is the sum of a symmetrically dispersed distribution of image noise and a secondary distribution at high μ_a due to the objects. This can be seen by considering the isosurface [see Fig. 3(a)] drawn at 1/2 maximum contrast.

There is generally a trade off between resolution and image noise. This is summarized in Fig. 5(a) where we plot FWHM-vs-image noise. The regularization constant param-

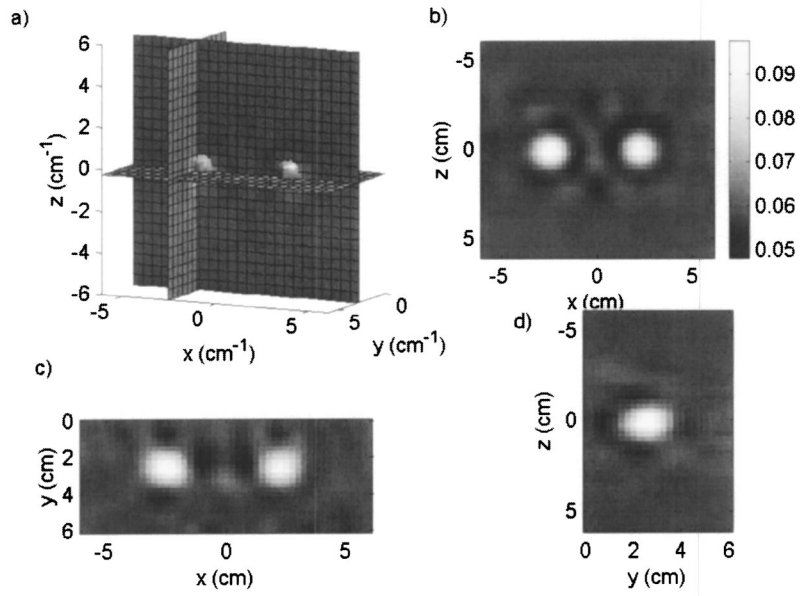

FIG. 3. Reconstruction of two point objects used for PSF measurements with $l_c=0.1$. (a) Three slices through the volume at $x=-2.5$ cm, $y=2.75$ cm, and $z=0.25$ cm, combined with an isosurface at half maximum contrast ($\mu_a=0.079$). (b) *xz*-plane slice at $y=2.75$ cm. (c) *xy*-plane slice at $z=0.25$. (d) *yz*-plane slice at $x=-2.5$ cm. Gray scale (units cm^{-1}) for all figures is shown in (b).

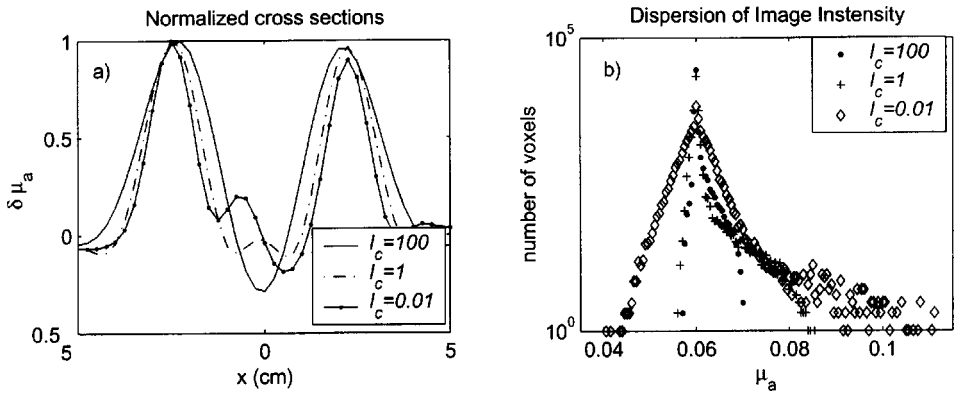

FIG. 4. (a) Cross-sections for three values of l_c. The resolution is improved for smaller values of l_c. (b) Image dispersion histograms for three values of l_c show the increase in image variance with decreasing values of l_c.

etrizes the curve. At a preliminary level of analysis the entire curve defines system performance. A viewer may choose to interpret the data at any point on the curve, trading resolution for image noise. However, it is preferable to establish the optimal image. There are several parameter choice methods for establishing the optimal regularization parameter. We considered three approaches.

An empirical approach is to define an image noise level that can be tolerated for a particular imaging question.[35] For instance, $\langle \delta\mu_a^2 \rangle^{1/2} \leqslant 0.0024$ would set the regularization constant at $l_c = 0.1$ and correspondingly the FWHM at 1.2 cm.

A parameter choice approach called L-curve analysis provides a method of effectively calculating the regularization constant directly from the measurements.[36] L-curve analysis examines the parametric relation between the image norm, the measurement error norm and the regularization constant. In Eq. (8) the regularization parameter, $\lambda(\mathbf{r})$, controls the relative weight between the image variance norm and the measurement error norm. L-curve analysis plots these two norms against each other for the range of regularization parameters [see Fig. 5(b)]. The result is an L shaped curve with the knee of the curve representing and optimal regularization value. This analysis places the regularization at $l_c = 1.0$.

Third, we considered an approach in which the ratio between the object contrast and the image noise (CNR) is maximized. Contrast is defined as peak $\delta\mu_a$ of the target and noise is defined as $\langle \delta\mu_a^2 \rangle^{1/2}$. We plot CNR versus the regularization constant in Fig. 5(c). The CNR peaks at $l_c = 0.1$. This corresponds to one decade lower than the L-curve analysis. Since the contrast-to-noise value is a more tangible optimization, we proceed with $l_c = 0.1$ as the optimal regularization constant. It appears that L-curve analysis provides an overly-smooth solution for the imaging situation of two isolated point objects in a relatively large imaging domain. When $l_c = 0.1$ we obtain a 3D point spread function with FWHM$=\{1.1,1.13,1.1\}$ cm obtained with an image noise of $\langle \delta\mu_a^2 \rangle^{1/2} = 0.0024$ cm^{-1}. Since the objects are 0.4 cm in diameter the peak contrast value is considerably lower than the physical target object contrast ($\delta\mu_{a\text{-recon}}/\delta\mu_{a\text{-object}} = 0.098/2 = 0.049$). However, the integrated signal Sig $= \delta\mu_a * \textit{volume}$ is closer to expectation with ($\text{Sig}_{\text{recon}}/\text{Sig}_{\text{object}} = 0.0265/0.0650 = 0.41$). Since the signal strength does not vary linearly with μ_a for large μ_a, this discrepancy in integrated signal strength is reasonable.

B. Characterization

Diffuse optical tomography is an inherently nonlinear imaging method. Although point spread functions are useful, one cannot be certain that a new object will show up as the original convolved with the PSF. It is therefore best to check questions of interest directly. In breast cancer studies one

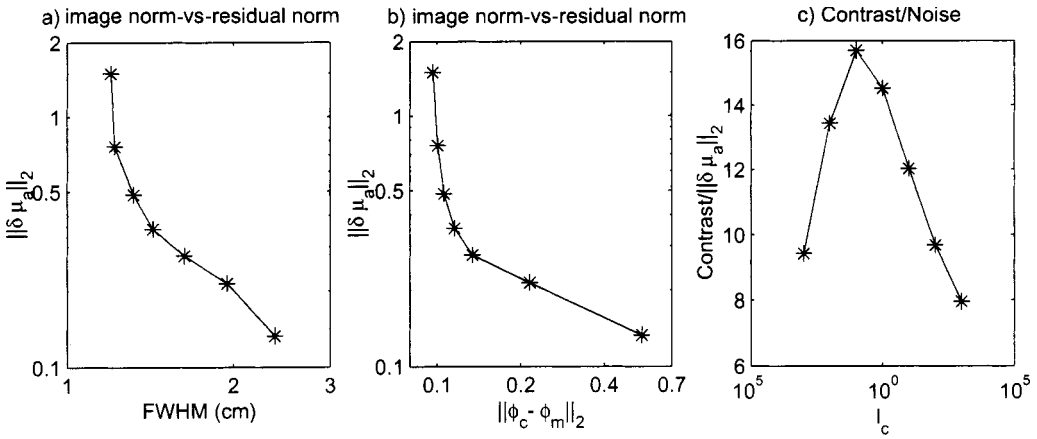

FIG. 5. (a) Image noise vs FWHM of PSF as a function of the regularization constant (l_c) for $l_c = \{1000,100,10,1,0.1,0.01,0.001\}$. (b) Image norm vs residual norm. (c) The ratio of (object contrast)/(image noise) as a function of l_c. The optimal regularization constant maximizes the contrast to noise ratio.

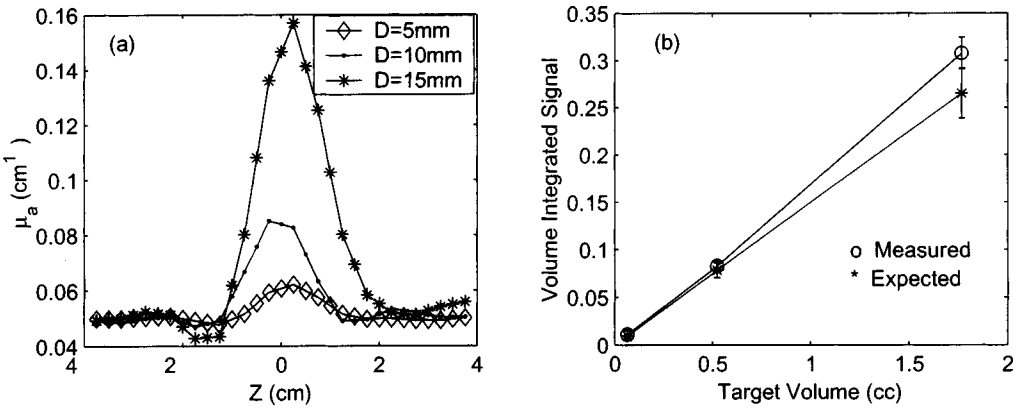

FIG. 6. A comparison of images of objects with different size (diameter={0.15,1.0,1.5} cm) and equivalent intrinsic contrast ($\delta\mu_a = 0.15$ cm^{-1}). (a) Cross-sections for the three objects show that the peak signal decreases for objects smaller than the PSF of the instrument. (b) A comparison of the volume integrated signal versus expected for an integration volume defined by 1.5* (FWHM of PSF).

aims to use DOT to characterize a suspicious mass. Our goal here is to evaluate whether the volume integrated signal is quantitative for objects smaller than the optimized PSF of the machine. This series of measurements evaluates the characterization of spherical objects with small differential contrast $\delta\mu_a/\mu_a = 3$. In particular, we reconstruct objects of three different sizes; 0.5 cm, 1.0 cm and 1.5 cm spheres, with $\mu_a = 0.2$. The results are shown in Fig. 6. The variance in the volume integrated signals was estimated using the variance in $\delta\mu_a$. Note that this method slightly over estimates the variance for objects larger than the PSF. The standard deviation in $\delta\mu_a$ was 0.0024 cm^{-1} or 12% of $\delta\mu_a$ whichever was greater. The image of the 1.5 cm sphere shows an object close to the correct size and with a moderately lower μ_a value, ($\delta\mu_{a\text{-recon}}/\delta\mu_{a\text{-object}} = 0.73$, $\text{Sig}_{\text{recon}}/\text{Sig}_{\text{object}} = 0.31/0.27 = 1.16$). Images of both the 0.5 cm target ($\delta\mu_{a\text{-recon}}/\delta\mu_{a\text{-object}} = 0.09$, $\text{Sig}_{\text{recon}}/\text{Sig}_{\text{object}} = 0.0011/0.009 = 1.16$) and 1.0 cm target ($\delta\mu_{a\text{-recon}}/\delta\mu_{a\text{-object}} = 0.23$, $\text{Sig}_{\text{recon}}/\text{Sig}_{\text{object}} = 0.083/0.078 = 1.06$) depict objects larger and with significantly lower μ_a than the targets, reflecting a smoothing operation consistent with the optimized PSF. However, the volume integrated signal of the objects show much better agreement with the expected values.

C. Field of view

In this section we evaluate the ability of the system to image an extended tissue volume and to reconstruct a heterogeneous medium with multiple objects. We dispersed 15 cubic silicon tissue phantom objects throughout the measurement volume. The 0.8 cm edge dimension cubes with $\mu_a = 0.2$ cm^{-1}, $\mu_s' = 10$ cm^{-1} were arranged in a hexagonal lattice. Single wavelength ($\lambda = 786$ nm) measurements were taken with and without the objects present and reconstructions were performed with $l_c = 0.1$. The resulting 3D reconstructed volume is depicted in Fig. 7 with isosurfaces at $\mu_a = 0.092$ cm^{-1}. The results are also shown in cross-sections at y depths of 1.5 cm, 3 cm, and 4.5 cm (Fig. 8). Note that the objects are well separated in all three dimensions and that only objects that belong in each plane are present. There is a small amount of ghosting between the slices, but this is consistent with the z-direction FWHM found in the point spread function. The peak values drop to 75% of the center values for objects on the edges of the reconstruction volume. The resolution is optimal at the central xz values and improves towards the source and detector plane. However, the spatially variant regularization has provided fairly consistent sensitivity and resolution throughout a volume with dimensions {16,6,5} cm.

D. Spectroscopy

The next set of measurements evaluate the ability to characterize the constituent concentrations of a tissue phantom. Two 3.2 cm^3 flow cells were used: one with an ink contrast and the other with an ICG contrast. Reconstructions were performed at all four wavelengths. The absorption maps were then combined into concentration maps on a voxel by

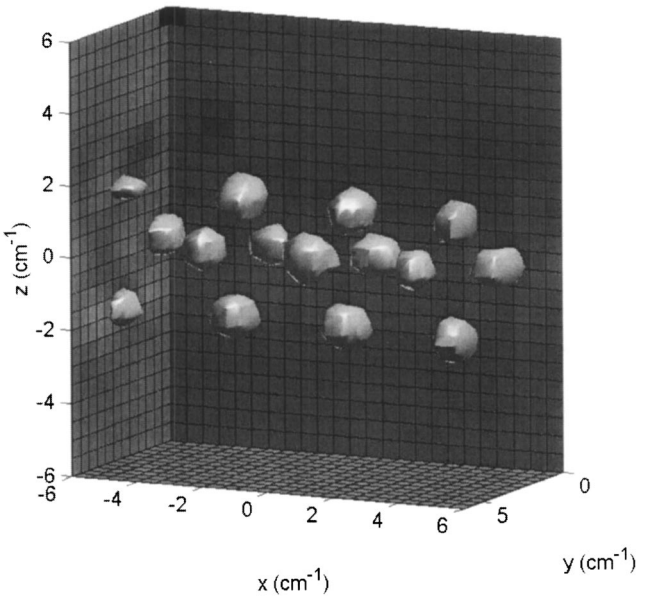

FIG. 7. A reconstruction of 15 objects indicates the spatial extent of the imaging domain of the instrument (field of view). Isosurfaces are drawn at 50% peak differential contrast.

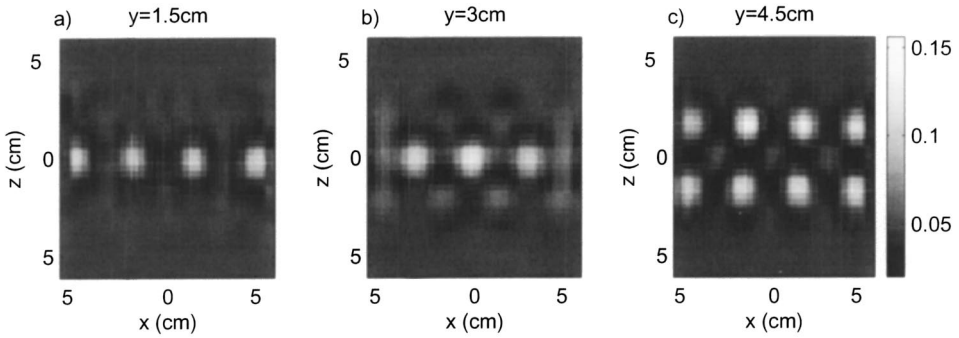

FIG. 8. Slices at three y values {1.5, 3, 4.5} through the 15 object reconstruction shown in Fig. 7.

voxel basis using $\vec{C}(\mathbf{r}_v)=E^{-1}\delta\vec{\mu}_a(\mathbf{r}_v)$. Here $\delta\vec{\mu}_a(\mathbf{r}_v)=\{\delta\mu_a(\mathbf{r}_v)^{\lambda 690}, \delta\mu_a(\mathbf{r}_v)^{\lambda 750}, \delta\mu_a(\mathbf{r}_v)^{\lambda 786}, \delta\mu_a(\mathbf{r}_v)^{\lambda 830}\}$, is a vector containing the $\delta\mu_a$ values at $\mathbf{r}_v$ for each wavelength, E is a matrix containing the extinction coefficients of ink, and indocyanine green at the four wavelengths, and $\vec{C}(\mathbf{r}_v)=\{[ICG](\mathbf{r}_v),[\mathrm{Ink}](\mathbf{r}_v)\}$ is a vector containing the concentrations at each voxel. The $\delta\mu_a$ and concentration images are shown in Fig. 9. Note that both objects appear in all four of the absorption images. However, the concentration images successfully distinguish between the india ink and the indocyanine green dye. The lower CNR in the ink image relative to the ICG image is due to the lower $\delta\mu_a$ of the ink target and results in a small artifact in the ink image at 60% of the maximum differential contrast. These results, combined with the object characterization results, suggest that even for tumors smaller than the resolution of our machine (diameter 0.5 cm), this DOT system will correctly determine the tissue chromophore concentrations when averaged over the volume of the PSF (e.g., the volume integrated values are correct). We anticipate similar spectral decomposition performance in obtaining ICG concentrations and hemoglobin concentrations in clinical imaging situations.

E. *In vivo* average breast properties

Transillumination images of a breast are shown in Fig. 10. The outline of the breast can be seen as well as superficial blood vessel structures on the detection plane. The breast position is obtained from these images. The average breast tissue properties are derived from the FD data at four wavelengths. The data was analyzed with a semi-infinite diffusion model.[39] The data and semi-infinite fits for a 25 year old subject are shown in Fig. 11. The variance in the measurements is less than the symbol size. The subset of source–detector pairs chosen sample a ~3 cm×5 cm region, central to the breast area shown in Fig. 10, to a depth of ~1.5 cm. We find good agreement with the semi-infinite model for the range of source–detector separations chosen. The absorption

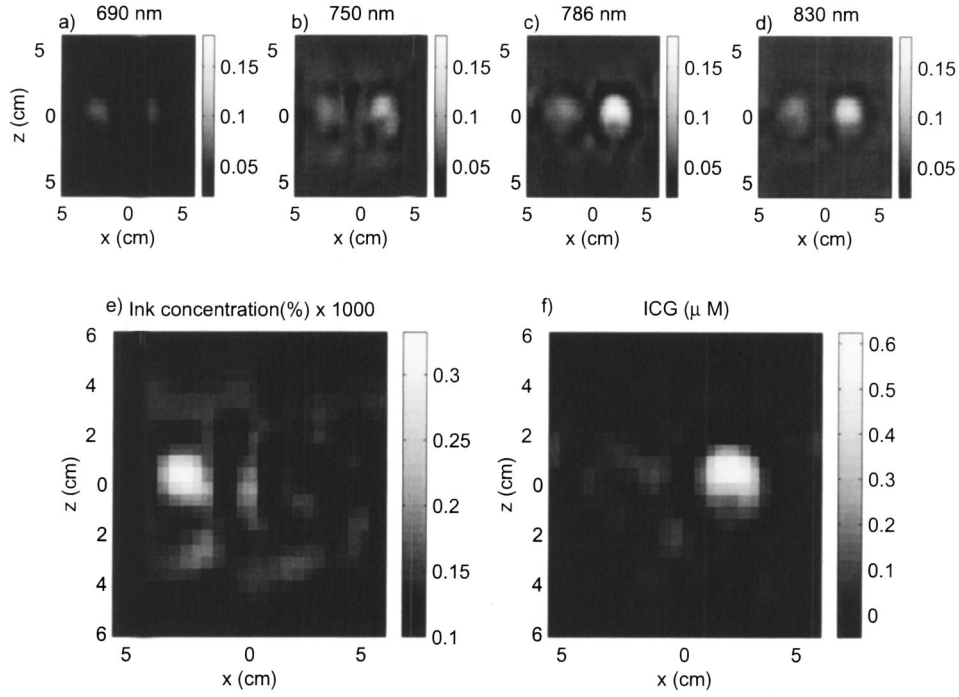

FIG. 9. (a)–(d) Absorption slice images at $y=3$ cm for four wavelengths (gray scale bar in units of cm^{-1}). (e), (f) Using spectral decomposition, the reconstructed concentrations of ICG and of India ink are obtained.

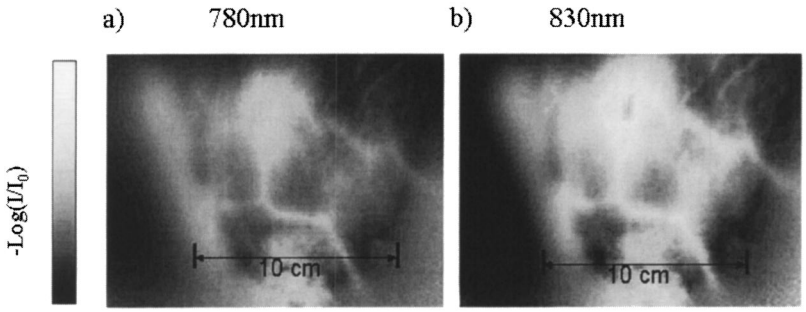

FIG. 10. (a), (b) Transillumination image obtained by summing images for all source positions for 690 nm and 830 nm, respectively. The outline of the breast is obtained from these pictures. Superficial blood vessels on the detection plane are visible.

and scattering coefficients obtained are plotted in Fig. 12. The error bars represent the standard deviation of the absorption and scattering coefficients from ten measurements. The hemoglobin concentrations were obtained through spectral decomposition assuming a 50/50 lipid/water concentration where the lipid spectra is from Ref. 40 and the water spectra is from Ref. 41. The resulting blood volume [HbT]=28 μM, and saturation, StO_2=63%, are consistent with values we have obtained using a scanning transmission RF machine.[31] Our numbers are also in reasonable agreement with the results of other groups using a variety of measurement types and geometries.[3,5,29]

The differential image experiments were reconstructed and yield the images shown in Fig. 13. The system is clearly capable of imaging tumor-like targets in the presence of physiologic fluctuations. The image has more structure than the Intralipid phantom images of equivalent targets (Fig. 3). This structure is most probably a result of physiologic fluctuations that propagate into the image as noise. We compare the dispersion of the voxel values for phantom and *in vivo* imaging in Fig. 14. The image variance in the *in vivo* measurements is 4.3 times larger than for Intralipid. This illustrates two points about the machine. First, the measurements obtained with the lens coupled CCD have sufficient SNR (i.e., instrument noise is not the leading cause of image noise for an *in vivo* measurement). Second, even in the presence of physiologic fluctuations on the time scale of minutes, we can produce images with large contrast-to-noise ratios.

IV. DISCUSSION

Diffuse optical tomography utilizes inherently 3D measurements of tissue volumes. In order for the technique to progress towards clinical utility it is important to develop instruments that provide full 3D imaging of the entire breast tissue volume. Furthermore, in such cases it becomes challenging to acquire and process a sufficiently large data set. In this paper we evaluated a novel hybrid CCD based DOT system with parallel computations for image reconstruction. This scheme provides imaging of liter tissue volumes with 0.5 cm voxel size and 1 cm resolution. Generally, when DOT systems use CCD detection, CCD elements are coupled to tissue surfaces using discrete fibers. We have demonstrated DOT performance using single lens coupling. This scheme has several advantages. Uncertainty in the calibration of the detectors coupling can often degrade image quality.[42] These coupling coefficients can be obtained at the cost of increasing the number of unknowns in the image reconstruction process. By using a single detection element and contact surface (imaging window) the number of calibration coefficients are significantly reduced (ideally to one detector coefficient). This is evident in the fact that the dominating systematic noise source in our device is the source fiber switching mechanism. The high resolution of the underlying CCD mea-

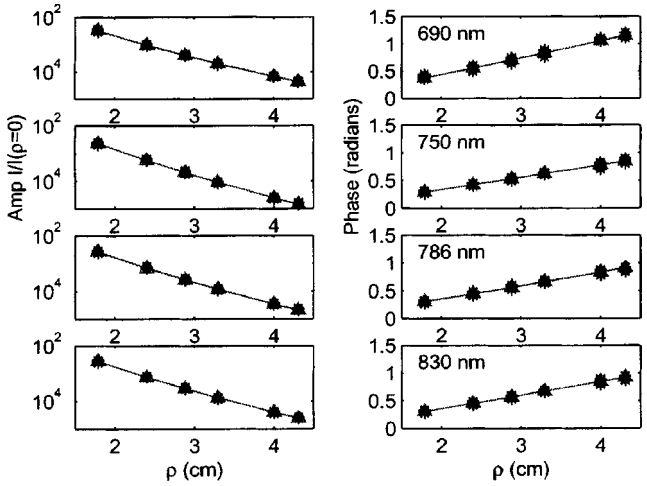

FIG. 11. Data and fits based on a semi-infinite diffuse wave solution to frequency domain data at 4 colors for measurements on human breast.

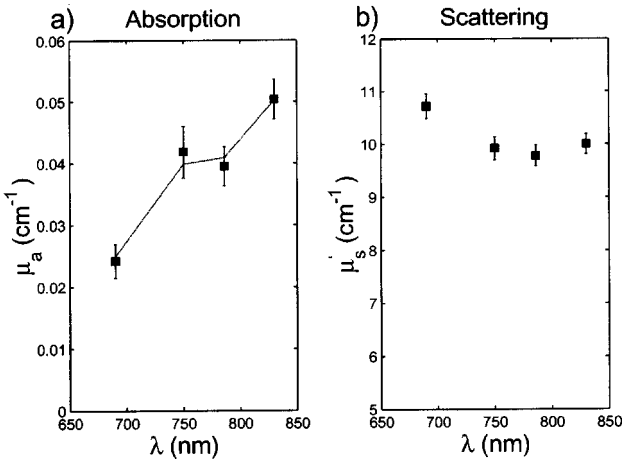

FIG. 12. Absorption and scattering coefficients for a healthy human breast.

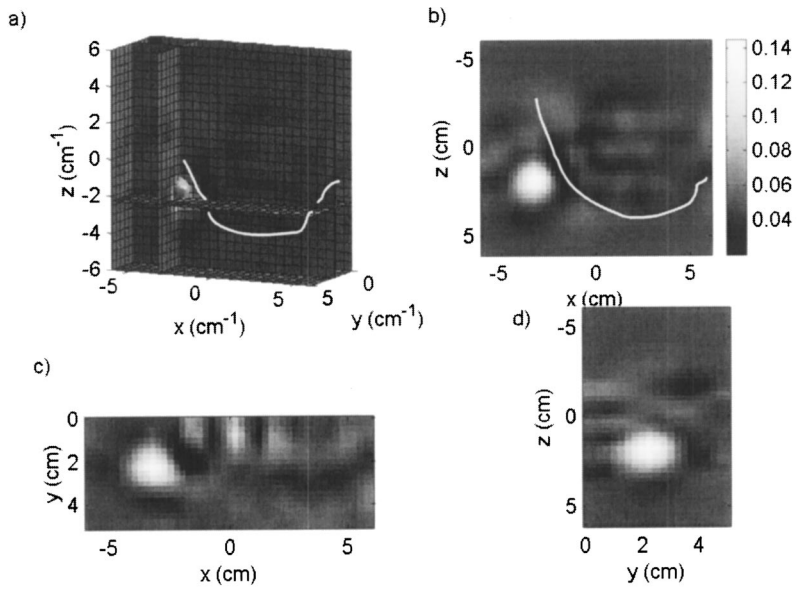

FIG. 13. Differential image reconstruction of a phantom target taped onto the surface of a human breast. These breast/phantom measurements extend the simpler intralipid studies to a more challenging situation. The background is no longer homogeneous but instead healthy breast tissue with both spatial and temporal variations in optical properties. (a) Three slices through the volume at $x=-2.5$, $y=2.75$, and $z=0.25$, combined with an isosurface at half maximum contrast ($\mu_a=0.083$). (b) *xz*-plane slice at $y=2.75$ cm. (c) *xy*-plane slice at $x=0.25$. (d) *yz*-plane slice at $x=-2.5$. Gray scale (units cm^{-1}) for all figures is shown in (b).

surement also facilitates two standard and relevant CCD features. The pixel binning is flexible allowing for an effortless exchange of detector area for sampling density, and the high resolution imaging permits a standard reflectance image of the breast from which the breast shape and particular boundary positions can be obtained. This knowledge can potentially be translated into *a priori* information for image reconstruction.

A second theme of this paper has been the characterization of our DOT device. To this end we employed an evaluation procedure that should have general relevance to DOT systems. Using tissue phantoms, we have evaluated the system for point spread function resolution, object characterization, multiple object tomography, field of view and spectral decomposition. A critical component of the evaluation procedure was the optimization of the relation between image noise and resolution for system parameters relevant to breast tumor imaging. Though the underlying physical models for DOT are nonlinear, we found that PSF derived generally describes the performance of the machine. This illustrates the manner in which DOT is ill-posed when constrained to absorption only perturbations. For absorption imaging, the ill-posed nature of DOT consists of a blurring process that can be conceptually and quantitatively captured in a simple localized point spread function characterization for most breast imaging situations. Related analytic studies by Schotland *et al.* explore similar point spread function use.[25]

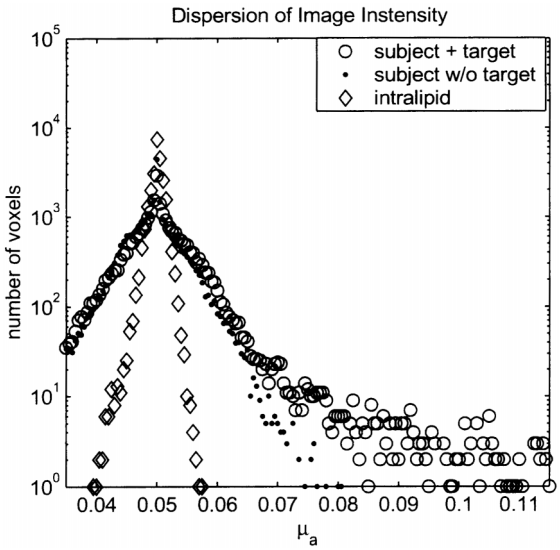

FIG. 14. Histogram of the voxel values for the *in vivo* phantom differential images. Three images are analyzed including (i) target on subject, (ii) baseline variance in subject measurements, and (iii) baseline variance in intralipid measurements.

For comparison with other groups we consider the ratio of the apparent object size (related to the FWHM of a PSF) divided by the depth of the object. We use this as an approximate measure of imaging performance with smaller ratios indicating better resolution. The system described in this paper obtains an object to depth ratio of 1/2.8. Jiang *et al.* have reconstructed three-dimensional images of tissue phantoms and tumors in breast.[4,19] Using a 16 source, 16 detector continuous wave instrument, 1.0 cm phantom objects were accurately reconstructed at a depth of 1.3 cm from the measurement surface giving an object to depth ratio of $<1/1.4$. The ratio may underestimate the resolution performance of their machine (i.e., they did not look at smaller objects). In addition, they have obtained a similar performance with *in vivo* images of tumors.[4] Pogue *et al.* have reported a considerable amount of work in two dimensions and recently explored the effects of three dimensions.[3,28,43,44] Using a 16 source, 16 detector frequency domain system 0.4 cm rods were correctly characterized at a depth of 2 cm (with an object contrast of 4:1). The resulting ratio of object to depth, 1/5, is very good. Note, these results are for cylinders which have higher integrated contrasts than spheres. When they look at spherical objects, the object contrast drops for sizes below 1.5 cm.[28] Hawrysz *et al.* have reconstructed three-

dimensional fluorescent objects with an error handling scheme using a 4 source, 46 detector system.[45] With this system, 1 cm objects were reconstructed at a depth of 2 cm giving an object to depth ratio of $<1/2$. Hebden *et al.* have used a 32 source, 32 detector time resolved system to reconstruct fairly low contrast objects and separate both absorption and scattering contrasts in a conical breast imaging geometry.[17] This is a particularly difficult imaging task. Here they find 1 cm objects reconstructed to twice the actual size (8 times larger volume) at a depth of 2.1 cm, resulting in an object to depth ratio of 1. Ueda *et al.*[1] also use a 32 source 32 detector time resolved system to image 1 cm^3 objects.[46] With objects at depths 1.0 cm, 3.0 cm, and 1.5 cm the system obtains FWHM values of 1.38, 2.03 and 2.35 cm. The resulting object/depth ratios were 1/0.72, 1/1.48 and 1/0.74, respectively. The different contrasts, data types and prior constraints concerning the absorption and scattering of objects, complicate comparisons across these different groups. We note though, that time–domain systems, perhaps due to system complexity, generally produce higher object/depth ratios than the cw and frequency–domain systems. Since time–domain systems inherently have more complete information, we anticipate time–domain performance to improve as systems become better optimized.

Finally *in vivo* studies of healthy subjects with our system evaluated repeatability of average tissue optical properties and differential imaging performance. These breast/phantom measurements extend the simple intralipid/phantom imaging tests to a considerably more challenging situation. The background is no longer homogeneous but instead is healthy breast tissue with both spatial and temporal variations in optical properties. It is critical to establish influence of the effects of normal fluctuations due to heart, respiration and slower fluctuations do not subject positions, temperature, etc. on image reconstruction. As it was not possible to place test imaging targets inside the breast we placed them on the breast surface. To maintain a reasonable DOT imaging challenge the objects were located in the center of the tank away from both the source and detector walls. Significantly the physiologic fluctuations, while degrading the image quality by a measurable amount, did not corrupt the general localizing capabilities. A small artifact is seen towards the source plane though the volume integrated signal is 1/10 that of the target. It is possible that recent methods for optode calibration may reduce this type of superficial artifact near the optode plates.[42] These experiments establish that the fluctuations that occur over a 6 minute measurement time increase the spatial variance or noise in DOT reconstructions by a factor of 4.3 over the spatial variance found in intralipid phantom measurements. However, targets with reasonable optical properties were still imaged. In addition these results suggest that the measurement noise has been sufficiently reduced and is not a limiting factor in the image reconstruction process for differential measurements. Based on these comprehensive evaluation studies we anticipate this system and systems of similar design will provide clinically useful quantitative 3D images of breast.

ACKNOWLEDGMENTS

We gratefully acknowledge support from Grants No. NIH RO1-CA75124-04, and Army BC9907335.

[a]Author to whom correspondence should be addressed. Electronic mail: jculver@nmr.mgh.harvard.edu
[b]Current address: Department of Radiology, Massachusetts General Hospital, Charlestown, Massachusetts 02129.

[1] D. A. Benaron, S. R. Hintz, A. Villringer, D. Boas, A. Kleinschmidt, J. Frahm, C. Hirth, H. Obrig, J. C. van Houten, E. L. Kermit, W. F. Cheong, and D. K. Stevenson, ''Noninvasive functional imaging of human brain using light,'' J. Cereb. Blood Flow Metab. **20**, 469–477 (2000).
[2] S. B. Colak, M. B. van der Mark, G. W. Hooft, J. H. Hoogenraad, E. S. van der Linden, and F. A. Kuijpers, ''Clinical optical tomography and NIR spectroscopy for breast cancer detection,'' IEEE J. Sel. Top. Quantum Electron. **5**, 1143–1158 (1999).
[3] B. W. Pogue, S. P. Poplack, T. O. McBride, W. A. Wells, K. S. Osterman, U. L. Osterberg, and K. D. Paulsen, ''Quantitative hemoglobin tomography with diffuse near-infrared spectroscopy: pilot results in the breast,'' Radiology **218**, 261–266 (2001).
[4] H. Jiang, Y. Xu, N. Iftimia, J. Eggert, K. Klove, L. Baron, and L. Fajardo, ''Three-dimensional optical tomographic imaging of breast in a human subject,'' IEEE Trans. Med. Imaging **20**, 1334–1340 (2001).
[5] V. Ntziachristos, A. G. Yodh, M. Schnall, and B. Chance, ''Concurrent MRI and diffuse optical tomography of breast after indocyanine green enhancement,'' Proc. Natl. Acad. Sci. U.S.A. **97**, 2767–2772 (2000).
[6] H. Wallberg, ''Diaphanography in various breast disorders. Clinical and experimental observations,'' Acta. Radiol. Diagn. **26**, 129–136 (1985).
[7] A. E. Profio, ''Scientific basis of breast diaphanography,'' Med. Phys. **16**, 60–65 (1989).
[8] X. H. Zhou, ''Detection of early breast cancer: an overview and future prospects,'' Crit. Rev. Biomed. Eng. **17**, 203–205 (1989).
[9] M. A. Franceschini, K. T. Moesta, S. Fantini, G. Gaida, E. Gratton, H. Jess, W. W. Mantulin, M. Seeber, P. M. Schlag, and M. Kaschke, ''Frequency-domain techniques enhance optical mammography: Initial clinical results,'' Proc. Natl. Acad. Sci. U.S.A. **94**, 6468–6473 (1997).
[10] M. J. Holboke, B. J. Tromberg, X. Li, N. Shah, J. Fishkin, D. Kidney, J. Butler, B. Chance, and A. G. Yodh, ''Three-dimensional diffuse optical mammography with ultrasound localization in a human subject,'' J. Biomed. Opt. **5**, 237–247 (2000).
[11] M. Gurfinkel, A. B. Thompson, W. Ralston, T. L. Troy, A. L. Moore, T. A. Moore, J. D. Gust, D. Tatman, J. S. Reynolds, B. Muggenburg, K. Nikula, R. Pandey, R. H. Mayer, D. J. Hawrysz, and E. M. Sevick-Muraca, ''Pharmocokinetics of ICG and HPPH-car for the detection of normal and tumor tissue using fluorescence, near-infrared reflectance imaging: A case study,'' Photochem. Photobiol. **72**, 94–102 (2000).
[12] R. Weissleder and U. Mahmood, ''Molecular imaging,'' Radiology **219**, 316–333 (2001).
[13] J. P. Culver, V. Ntziachristos, M. J. Holboke, and A. G. Yodh, ''Optimization of optode arrangements for diffuse optical tomography: A singular-value analysis,'' Opt. Lett. **26**, 701–703 (2001).
[14] M. Patterson, B. Chance, and B. Wilson, ''Time resolve reflectance and transmittance for the noninvasive measurement of tissue optical properties,'' Appl. Opt. **28**, 2331–2336 (1989).
[15] S. R. Arridge and W. R. B. Lionheart, ''Nonuniqueness in diffusion-based optical tomography,'' Opt. Lett. **23**, 882–884 (1998).
[16] V. Ntziachristos, B. Chance, and A. G. Yodh, ''Differential diffuse optical tomography,'' Opt. Express **5**, 230–242 (1999).
[17] J. C. Hebden, H. Veenstra, H. Dehghani, E. M. C. Hillman, M. Schweiger, S. R. Arridge, and D. T. Delpy, ''Three-dimensional time-resolved optical tomography of a conical breast phantom,'' Appl. Opt. **40**, 3278–3287 (2001).
[18] E. M. Hillman, J. C. Hebden, M. Schweiger, H. Dehghani, F. E. Schmidt, D. T. Delpy, and S. R. Arridge, ''Time resolved optical tomography of the human forearm,'' Phys. Med. Biol. **46**, 1117–1130 (2001).
[19] H. B. Jiang, Y. Xu, and N. Iftimia, ''Experimental three-dimensional optical image reconstruction of heterogeneous turbid media from continuous-wave data,'' Opt. Express **7**, 204–209 (2000).
[20] C. H. Schmitz, H. L. Graber, H. B. Luo, I. Arif, J. Hira, Y. L. Pei, A. Bluestone, S. Zhong, R. Andronica, I. Soller, N. Ramirez, S. L. S. Barbour, and R. L. Barbour, ''Instrumentation and calibration protocol for

imaging dynamic features in dense-scattering media by optical tomography,'' Appl. Opt. **39**, 6466–6489 (2000).
[21] T. O. McBride, B. W. Pogue, S. Jiang, U. L. Osterberg, and K. D. Paulsen, ''A parallel-detection frequency–domain near-infrared tomography system for hemoglobin imaging of the breast *in vivo*,'' Rev. Sci. Instrum. **72**, 1817–1824 (2001).
[22] K. T. Moesta, S. Totkas, S. Fantini, H. Jess, M. Kaschke, and P. M. Schlag, ''Frequency domain laser scanning mammography of the breast—First clinical evaluation study,'' Eur. J. Cancer **33**, 358 (1997).
[23] X. D. Li, D. N. Pattanayak, T. Durduran, J. P. Culver, B. Chance, and A. G. Yodh, ''Near-field diffraction tomography with diffuse photon density waves,'' Phys. Rev. E **61**, 4295–4309 (2000).
[24] V. A. Markel and J. C. Schotland, ''Inverse problem in optical diffusion tomography. I. Fourier–Laplace inversion formulas,'' J. Opt. Soc. Am. A **18**, 1336–1347 (2001).
[25] J. C. Schotland and V. A. Markel, ''Inverse scattering with diffusing waves,'' J. Opt. Soc. Am. A **18**, 2767–2772 (2001).
[26] S. R. Arridge, ''Optical tomography in medical imaging,'' Inverse Probl. **15**, R41–R93 (1999).
[27] B. W. Pogue, M. S. Patterson, H. Jiang, and K. D. Paulsen, ''Initial assessment of a simple system for frequency-domain diffuse optical tomography,'' Phys. Med. Biol. **40**, 1709–1729 (1995).
[28] B. W. Pogue, S. Geimer, T. O. McBride, S. D. Jiang, U. L. Osterberg, and K. D. Paulsen, ''Three-dimensional simulation of near-infrared diffusion in tissue: boundary condition and geometry analysis for finite-element image reconstruction,'' Appl. Opt. **40**, 588–600 (2001).
[29] N. Shah, A. Cerussi, C. Eker, J. Espinoza, J. Butler, J. Fishkin, R. Hornung, and B. Tromberg, ''Noninvasive functional optical spectroscopy of human breast tissue,'' Proc. Natl. Acad. Sci. **98**, 4420–4425 (2001).
[30] V. Quaresima, S. Matcher, and M. Ferrari, ''Identification and quantification of intrinsic optical contrast for near-infrared mammography,'' Photochem. Photobiol. **67**, 4–14 (1998).
[31] T. Durduran, R. Choe, L. Zubkov, B. Chance, and A. Yodh, ''Bulk optical properties of healthy female tissue,'' Phys. Med. Biol. **47**, 2847–2861 (2002).
[32] Y. S. Yang, H. L. Liu, X. D. Li, and B. Chance, ''Low-cost frequency–domain photon migration instrument for tissue spectroscopy, oximetry, and imaging,'' Opt. Eng. **36**, 1562–1569 (1997).
[33] C. P. Gonatas, M. Ishii, J. S. Leigh, and J. C. Schotland, ''Optical diffusion imaging using a direct inversion method,'' Phys. Rev. E **52**, 4361–4365 (1995).
[34] J. C. Hebden, D. J. Hall, M. Firbank, and D. T. Delpy, ''Time-resolved optical imaging of a solid tissue-equivalent phantom,'' Appl. Opt. **34**, 8038–8047 (1995).
[35] M. A. Oleary, D. A. Boas, B. Chance, and A. G. Yodh, ''Experimental images of heterogeneous turbid media by frequency–domain diffusing-photon tomography,'' Opt. Lett. **20**, 426–428 (1995).
[36] H. W. Engl, M. Hanke, and A. Neubauer, *Regularization of Inverse Problems* (Kluwer Academic, Dordrecht, 1996), pp. 116–125.
[37] B. W. Pogue, T. O. McBride, J. Prewitt, U. L. Osterberg, and K. D. Paulsen, ''Spatially variant regularization improves diffuse optical tomography,'' Appl. Opt. **38**, 2950–2961 (1999).
[38] R. Groenhuis, H. Ferwerda, and J. Tenbosch, ''Scattering and absorption of turbid materials determined from reflection measurements. 1. Theory,'' Appl. Opt. **22**, 2456–2462 (1983).
[39] R. C. Haskell, L. O. Svaasand, T. T. Tsay, T. C. Feng, and M. S. McAdams, ''Boundary-conditions for the diffusion equation in radiative-transfer,'' J. Opt. Soc. Am. A **11**, 2727–2741 (1994).
[40] R. Cubeddu, ''Effects of the menstrual cycle on the red and near-infrared optical properties of the human breast,'' Photochem. Photobiol. **72**, 383–391 (2000).
[41] G. Hale and M. Querry, ''Optical constants of water in the 200 nm 200 μm region,'' Appl. Opt **12**, 555–563 (1973).
[42] D. Boas, T. Gaudette, and S. Arridge, ''Simultaneous imaging an optode calibration with diffuse optical tomography,'' Opt. Express **8**, 263–270 (2001).
[43] T. O. McBride, B. W. Pogue, S. D. Jiang, U. L. Osterberg, K. D. Paulsen, and S. P. Poplack, ''Initial studies of *in vivo* absorbing and scattering heterogeneity in near-infrared tomographic breast imaging,'' Opt. Lett. **26**, 822–824 (2001).
[44] B. W. Pogue, C. Willscher, T. O. McBride, U. L. Osterberg, and K. D. Paulsen, ''Contrast-detail analysis for detection and characterization with near-infrared diffuse tomography,'' Med. Phys. **27**, 2693–2700 (2000).
[45] D. J. Hawrysz, M. J. Eppstein, J. W. Lee, and E. M. Sevick-Muraca, ''Error consideration in contrast-enhanced three-dimensional optical tomography,'' Opt. Lett. **26**, 704–706 (2001).
[46] Y. Ueda, K. Ohta, M. Oda, M. Miwa, Y. Tsuchiya, and Y. Yamashita, ''Three-dimensional imaging of a tissuelike phantom by diffusion optical tomography,'' Appl. Opt. **40**, 6349–6355 (2001).